

# Polarimetry at millimeter wavelengths with the NIKA camera: calibration and performance

Address(es) of author(s) should be given

Preprint online version: November 18, 2015

## Abstract

Constraint observationally the magnetic field role in the star formation process is one of the outstanding problem in millimeter and sub-millimeter astronomy. In this context observations of galactic regions will be carried out with the 1.25 mm polarization channel of the dual-band *NIKA2* camera, based on Lumped Element Kinetic Inductance Detectors (LEKIDs) and installed at the IRAM 30-meter telescope (Granada, Spain) on October 2015. *NIKA2* observes the sky at 1.25 mm and 2.05 mm corresponding at the central frequency of 260 and 150 GHz and it has polarization capability at 260 GHz. The polarization setup in the *NIKA2* camera consists of a rotating achromatic half wave plate (AHWP) placed at 300K in front of the cryostat window and a polarizer mounted in the 100 mK stage of the cryostat in order to split the two orientations of the linear polarization on two matrix of thousands of pixels. A polarizer is necessary because of the LEKIDs Hilbert geometry, which is intrinsically not sensitive to the polarization.

In order to test the performance of this system we used the prototype of *NIKA2*, *NIKA*, which consists of two arrays of 132 and 224 detectors LEKIDs observing at same frequencies. The *NIKA* polarization system (AHWP + polarizer) is placed at 300K in front of the *NIKA* cryostat window. The combined action of the continuously rotating AHWP and the small time constant of the LEKIDs permits the simultaneous measurements of the three Stokes parameters (I, Q, U) on a same area of the sky.

We had two technical campaign in order to test the system and study systematics effects on January 2014 and October 2014. This paper aims to discuss the laboratory characterization of the instrumental setup, the polarized data reduction analysis and the calibration effectuated on several quasars and calibration extended sources observed during the observational campaign on February 2015. In particular we found a polarization angle at 260 GHz and 150 GHz, respectively, of  $\alpha_{sky} = (-89.3 \pm 3.2)^\circ$  and  $\alpha_{sky} = (-74.1 \pm 3.9)^\circ$  for the quasar 3C273,  $\alpha_{sky} = (29.0 \pm 3.9)^\circ$  and  $\alpha_{sky} = (27.7 \pm 3.9)^\circ$  for the primary calibration source, the quasar 3C286 and  $\alpha_{sky} = (35.9 \pm 3.2)^\circ$  and  $\alpha_{sky} = (31.9 \pm 3.6)^\circ$  for the quasar 3C279. We also observed the crab nebula, Orion-OMC1, M87 and Cygnus A. The averaged polarization angle in the OMC1 region of the Orion molecular cloud is  $\alpha_{sky} = (21.3 \pm 3.6)^\circ$  and  $\alpha_{sky} = (22.1 \pm 2.6)^\circ$  at 2.05 and 1.25 mm, respectively.

**Key words.** Techniques: Polarization – KIDs – individual: NIKA

## 1. Introduction

Interstellar dust plays a key role in the Milky Way and more generally in the evolution of galaxies, since it governs a number of physical and chemical processes in the interstellar medium (ISM). Dust polarization observations can be used to define the magnetic field direction projected onto the plane of sky, thus complementing our knowledge of the Galactic magnetic field, obtained via measurements of Faraday rotation, synchrotron emission and Zeeman splitting. Magnetic fields provide the pressure balance required to support the ISM against gravitational collapse on large scales, regulating the filamentary structures observed within molecular clouds (Fiege & Pudritz 2000). While these magnetic fields remain a large part of the galaxy dynamics, the origins of these fields are not well understood. Since the degree of dust continuum polarized emission is low (typically 5% - (Matthews et al. 2002)), a systematic polarimetric study of nearby star-forming filaments and pre-stellar cores requires a fast mapping speed, a high resolution and a large FoV (Field of View) foreseen in *NIKA2*. *NIKA2* is a high resolution camera (18.5 arcsec at 150 GHz and 11 arcsec at 260 GHz) based on thousands of Lumped Element Kinetic Inductance Detectors (LEKIDs) observing the sky at 260 GHz and 150 GHz from the IRAM 30 m telescope in the Sierra Nevada (Spain). It has been installed on October 2015 at the telescope and will be opened to the astronomers on late 2016.

A key scientific objective for the 260 GHz polarization channel of the *NIKA2* camera would be to clarify the role played by magnetic fields in the star formation process. The *NIKA2* polarimeter consists of a rotating multi-layer half wave plate (HWP) placed in front of the cryostat window and a polarizer to split the two orientations of the linear polarized light on two matrix mounted in the 100 mK stage of the dilution cryostat used to cool down the detectors LEKIDs at their optimal functioning temperature. This camera has replaced the already successful prototype *NIKA* camera (Catalano et al. 2014) (Adam et al. 2014) opened to external observers in February 2014. With respect to the prototype, *NIKA2* will cover the IRAM 30 m telescope focal plane with a FoV of 6.5 arcminutes and will improve in mapping speed and sensitivity. The study of the performance of the polarimeter has been done with the *NIKA* prototype during the last two years. In *NIKA* the polarized system (HWP + polarizer) is placed at 300K in front of the cryostat window. The paper is organized as follows, section 2 presents the instrument and the polarization facilities; section 3 presents the results from the instrumental characterization in laboratory; section 4 presents the characterization of the instrument at the telescope; section ?? presents the polarization pipeline data reduction software; section 6 the results on photometric calibration and polarized calibration provided on several quasars; section 7 presents the polarization maps on few extended sources, Orion OMC-1, M87 and CygnusA.

## 2. NIKA Instrument

The *NIKA* camera (Monfardini et al. 2010) consists of two arrays with LEKIDs with maximum transmission at 150 and 260 GHz. The LEKIDs are a type of superconducting photon detector. Photons are detected by measuring the change in quasi-particle density caused by the splitting of Cooper pairs in the superconducting resonant element. This change in quasi-particle density alters the kinetic inductance, and hence the resonant frequency of the resonant element (Doyle et al. 2008). The respective angular resolutions (FWHM) are 18.5 arcsec and 12.5 arcsec. The cryostat is a major tool of the *NIKA* instrument, the two KID arrays of hundreds pixels are cooled down to their optimal temperature of  $\sim 100$  mK. This is achieved by a 4 K cryocooler and a closed-cycle  $^3\text{He}$  -  $^4\text{He}$  dilution. The optical coupling between the telescope and the detectors is made by warm aluminium mirrors and cold refractive optics (Catalano et al. 2014).

### 2.1. NIKA POLARIMETER

The instrumental setup for polarization measurements consists of a rotating Half Wave Plate (HWP) and a subsequent polarizer as schematically illustrated in fig. 1, the system is placed in front of the cryostat window at 300K (see fig. 4). The dependence of the phase shift on wavelength constitutes an intrinsic limit in designing a HWP operating in a broad spectral range. In order to have a maximum transmission of the polarized signal in the broad spectral range of *NIKA*, we chose a multi-layer HWP Savini et al. (2006). This is conceived to compensate and keep the phase shift approximately constant across the bandwidth, by stacking several layers of birefringent substrates, which are rotated with respect to each other about their optical axes by a frequency-dependent set of angles. A two-layers broadband anti-reflection coating has been added to maximise the in-band transmission of the HWP and it has been also hot-pressed to the front and back surfaces of the assembled plate. The polarizer is necessary because of the LEKID Hilbert geometry (Roesch et al. 2012) that make the pixels sensitive to both orientations of the linear polarization.

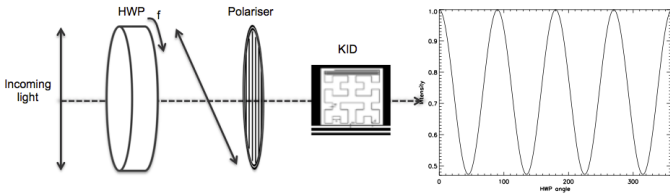


**Figure 1.** Observational polarimeter scheme.

## 3. Laboratory characterization

In order to estimate the performance of the whole polarization chain and the contribution from any instrumental polarization we have performed a laboratory characterisation. In order to

characterize the spectral transmission of the system we used a polarizing Martin Puplett type Fourier-Transform-Spectrometer, the HWP in a fixed position and the dilution cryostat that cools down the optics and KIDs to 100 mK, see the fig. 2. The Martin-Puplett produces the difference between the powers of two input polarised beams which are built by two black bodies at different temperatures (ambient eccosorb and warmed eccosorb) modulated by a rotating wire-grid.

We assume to use an ideal polarizer so we will focus only on the characterisation of the HWP parameters. By rotating the HWP angle, we expect to observe a different attenuation for each wavelength due to the linear relation between the phase shift and the wavelength. This effect is expected to be quite weak because the HWP is achromatic.

First we measured a spectrum with the HWP aligned to its ordinary axis. This corresponds to the maximum signal in which we expect to have no distortion of the *NIKA* bandpass. We used this measured spectrum as a reference spectrum to an analytical model based on the Mueller formalism, Eq. 1, that takes into account for the optical devices.

Rotating the HWP we found an attenuation as shown in fig. 3, here the maximum transmission is represented by the spectrum at about  $46.8^\circ$  with respect to the HWP zero. Creating a model accounting for a realistic HWP Mueller matrix 1 (Savini et al. 2006) we can derive the HWP parameters.  $\alpha$  and  $\beta$  are the transmission coefficients of the orthogonal polarizations aligned with the birefringent axes.  $\theta$  is the angle of the incident polarization with respect to the reference frame defined by these axes and  $\phi$  is the phase shift introduced by the plate between the orthogonal polarizations. In this model we use the phase shift  $\phi$  optimized at each wavelength of the *NIKA* band-pass provided by Cardiff University. Fitting the observed attenuated spectra, we find the values  $\alpha$  and  $\beta$  of 1 and 0.98 at 1.15 mm and 0.98 and 0.92 at 2.05 mm. Once the  $\alpha$ ,  $\beta$  and  $\phi$  parameters are determined we can derive the polarization efficiency  $\rho_{\text{pol}}$ . From Eq. 1 we can define the HWP polarization efficiency as  $\rho_{\text{pol}} = (1 - 2\gamma)/2$  where  $\gamma = \frac{\alpha\beta \cos(\phi)}{\alpha^2 + \beta^2}$ . We find  $\rho_{\text{pol}} \approx 1$  almost constant in the *NIKA* band, so we observe a transmission of 100 % in polarization.

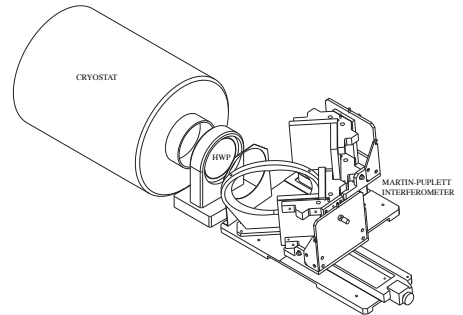


**Figure 2.** Laboratory instrumental setup. From left to right, the *NIKA* cryostat, the HWP in a fixed position and a Martin-Puplett interferometer.

$$M_{HWP} = \begin{pmatrix} \alpha^2 + \beta^2 & (\alpha^2 - \beta^2) \cos 2\theta & (\alpha^2 - \beta^2) \sin 2\theta \\ (\alpha^2 - \beta^2) \cos 2\theta & (\alpha^2 + \beta^2) \cos^2 2\theta + 2\alpha\beta \sin^2 2\theta \cos \phi & (\alpha^2 + \beta^2 - 2\alpha\beta \cos \phi) \cos 2\theta \sin 2\theta \\ (\alpha^2 - \beta^2) \sin 2\theta & (\alpha^2 + \beta^2 - 2\alpha\beta \cos \phi) \cos 2\theta \sin 2\theta & (\alpha^2 + \beta^2) \sin^2 2\theta + 2\alpha\beta \cos^2 2\theta \cos \phi \end{pmatrix} \quad (1)$$

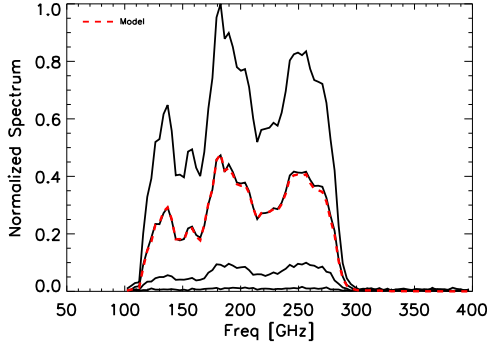


**Figure 3.** Maximum transmission at an angle of  $46.8^\circ$  respect to the HWP zero and attenuated spectra at  $72^\circ$ ,  $79^\circ$ ,  $86.4^\circ$  (top curve to bottom curve). For example, the model (red dotted line) fits the spectrum at an angle of  $72^\circ$ .

#### 4. Observation strategy

In order to extract the polarized signal from the unpolarized foreground it is common to use the modulation/demodulation technique. By means of a polarization modulator, the half-wave plate, the polarized component of the incoming radiation is modulated at a precise frequency. If the modulation acts only on the Q and U Stokes parameters of the radiation, the intensity of the latter will be unchanged, at least in the ideal case. Since KIDs are incoherent detectors, they are not sensitive to the phase of the wave but only to its intensity. We need to insert a linear polarizer along the optical path to translate the modulation of the Stokes parameters into a modulation of the total intensity of the transmitted wave. For more details see (Siringo et al. 2004).

The polarization setup as mounted in the cabin of the telescope is represented by a schematic design in the fig. 4. The linearly polarized signal arrives by the last mirror of the telescope optics and it passes through the HWP, rotating at  $\sim 2.98$  Hz, and the subsequent polarizer and finally it is detected by the two matrix of LEKIDs placed inside the cryostat.

This technique allows the quasi-simultaneous measurements of the three Stokes parameters ( $I$ ,  $Q$ ,  $U$ ) on a given sky position. The data output are expected modulated at four times the mechanical rotation frequency of the HWP. The rotation speed was chosen in order to produce 12 measurements per mechanical tour of the step motor synchronised to the sampling frequency that is 47.6837 Hz. This recovers 3 samples per optical tour which is still enough to reconstruct  $I$ ,  $Q$ ,  $U$  Stokes parameters. Thus, the signal is extracted using a lock-in procedure around the fourth harmonic of this frequency. The expected signal measured by a KID  $k$  is:

$$m_k = \frac{1}{2} \{ I + \rho_{\text{pol}} [Q \cos(4\omega t + 2\alpha_{\text{Sky}}(p(t))) + U \sin(4\omega t + 2\alpha_{\text{Sky}}(p(t)))] \} \quad (2)$$

where  $\rho_{\text{pol}}$  is the polarisation efficiency. In real conditions there is an additional parasitic signal at harmonics of  $1\omega$ ,  $2\omega$ ,  $3\omega$  due to imperfections of the HWP and the atmospheric and electronic noise to take into account. Accounting for these parasitic signals and for the atmospheric and electronic noise eq. (2) reads:

$$m_k = \frac{1}{2} [I + \rho_{\text{pol}} Q \cos(4\omega t + 2\alpha_{\text{Sky}}(p(t))) + \rho_{\text{pol}} U \sin(4\omega t + 2\alpha_{\text{Sky}}(p(t))) + S_{\text{parasitic}}(\omega t, 2\omega t, 3\omega t, \dots)] + \text{atmosphere} + \text{noise}_{\text{detector}} \quad (3)$$

where  $p(t)$  represents the pointing matrix and  $\alpha_{\text{Sky}}$  the angle between the telescope reference frame and the local meridian on the sky. The angle  $\alpha_{\text{Sky}}$  is measured from north to east in the equatorial system as  $\alpha_{\text{Sky}} = \tau - \epsilon - \eta$ , where  $\epsilon$  represents the elevation,  $\eta$  the parallactic angle, and  $\tau = 45.54^\circ$  is the tilt of the switch mirror of the Nasmyth system along the elevation axis, which creates an angular offset of the image of the sky on the detectors arrays. We discuss the data reduction pipeline from the raw signal to maps in the section 5.

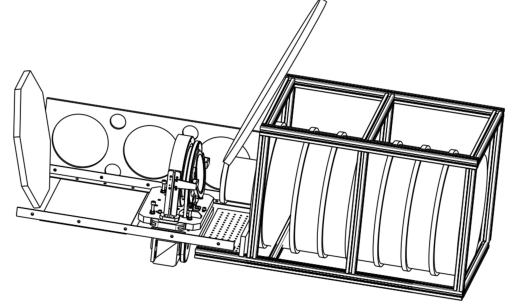


**Figure 4.** Telescope instrumental setup. From left to right the last mirror of the telescope optics, the motor step within the achromatic HWP and the polariser inclined by  $\sim 10$  degrees in front of the NIKA cryostat window.

#### 5. Data analysis

In order to calibrate, filter, and process data onto sky maps we developed a dedicated reduction pipeline (Catalano et al. 2014), (Adam et al. 2014). The main steps of the processing consist of:

- read data time ordered information (TOI): the data are ordered per kid and regularly sampled with time.
- TOI calibration: the absolute calibration is applied to these TOIs and an atmospheric absorption correction performed.
- atmospheric and electronic noise decorrelation: depending on the scientific target, two basic decorrelation methods are used, a dual-band decorrelation using a specific channel to obtain a template of the atmospheric emission and a single-band decorrelation where a sky noise TOI template is produced by averaging all TOIs of a single array. In both cases we prefer mask the source to select the pixels far from the source to reconstruct the subtraction template.
- map-making: projection of the TOIs of a same frequency band on a pixelized map.

An accurate calibration process is required to define the impact of the systematic errors on the final maps. The planet Uranus is the primary calibrator for the NIKA absolute calibration. The calibration factor is derived by fitting a Gaussian of fixed angular size on the reconstructed maps of Uranus (Catalano et al. 2014). The sky maps are corrected for the atmospheric contribution rescaling the observed signal by what that would be obtained in the absence of the atmosphere. This is achieved via the elevation scan technique (*skydip*). The NIKA atmospheric calibration consist in measuring the variation in the resonance frequencies of the detectors versus the airmass via elevation scans (*skydip* (Dicke

et al. 1946)) from 65 to 20 degrees above the horizon. This procedure permits to use *NIKA* instrument itself as a tau-meter (Catalano et al. 2014).

### 5.1. Polarization specific data analysis

In order to analyse the polarized data output we have developed a dedicated polarization data reduction pipeline.

$I$ ,  $Q$ ,  $U$  Stokes parameters maps in sky coordinates are constructed by applying the following procedures:

- construction of a template of the HWP modulation and removal of parasitic signal at harmonics of  $\omega$ ;
- construction of  $Q$  and  $U$  TOIs (time ordered informations) from the  $4\omega$  component using a modulation/demodulation technique.
- removal of atmospheric noise both in intensity and polarization;
- projection of the  $I$ ,  $Q$ ,  $U$  TOIs into  $I$ ,  $Q$ ,  $U$  maps.

Atmospheric emission dominates at low frequencies with a  $1/f$  like spectrum but the modulation of the polarized signal imposed by the HWP combined with the scanning strategy allows us to shift the astrophysical signal away from the largest atmospheric contribution (Johnson et al. 2007). Nevertheless the time ordered data contain a significant instrumental signal which is synchronous with the rotation of the HWP, as shown in fig. 5. The HWP synchronous signal is estimated and subtracted from the raw data, producing the time-ordered information (TOI). The time-ordered polarization information (TOIP) are extracted from the TOI by demodulation using a phase-locked at the frequency of  $4\omega$ . In the fig. 5 we can identify the atmospheric noise and the parasitic synchronous signal at all harmonics of the mechanical rotational frequency  $\omega$ . The Stokes vector  $I$  power spectrum in fig. 6 (top) shows a noise described by a function  $1/f^\beta$  with  $\beta \sim -1.2$ . Instead we find a flat spectrum looking at the power spectra for polarization data  $Q$  and  $U$  (fig. 6), with only a white noise component, as expected.

For map making, the demodulation procedure also includes a band-pass filter with high and low-pass edges at 0.01 and 2.9 Hz, respectively, that is used to reject any out-of-band signals. In order to make a  $n_{pix}$  map, all samples must be taken into account to include noise correlations (in time and from pixel to pixel) (Benoît et al. 2004). The equation 2 is generalized to:

$$\mathbf{M} = \mathcal{A}\mathbf{S} + \mathbf{N} \quad (4)$$

where  $\mathbf{M}$  is the time ordered vector of  $n_t \times n_{kid}$  measures,  $\mathbf{S}$  the  $(3 \times n_{pix})$  - vector Stokes map of the sky,  $\mathcal{A}$  the pointing matrix and  $\mathbf{N}$  the  $n_t \times n_{kid}$  noise vector. The  $\chi^2$  is given by

$$\chi^2 = (\mathbf{M} - \mathcal{A}\mathbf{S})^T \mathcal{N}^{-1} (\mathbf{M} - \mathcal{A}\mathbf{S}) \quad (5)$$

and is minimised by the solution

$$\mathbf{S} = (\mathcal{A}^T \mathcal{N}^{-1} \mathcal{A})^{-1} \mathcal{A}^T \mathcal{N}^{-1} \mathbf{M} \quad (6)$$

The covariance matrix is

$$\Sigma = (\mathcal{A}^T \mathcal{N}^{-1} \mathcal{A})^{-1} \quad (7)$$

When the noise is not correlated from one measurement to another,  $\mathcal{N}$  is diagonal and the inversion of large matrices can be solved. We therefore consider each pixel individually, computing the  $(3,3)$ - matrix  $\mathcal{A}^T \mathcal{N}^{-1} \mathcal{A}$  and the  $(3)$ -vector  $\mathcal{A}^T \mathcal{N}^{-1} \mathbf{M}$ .

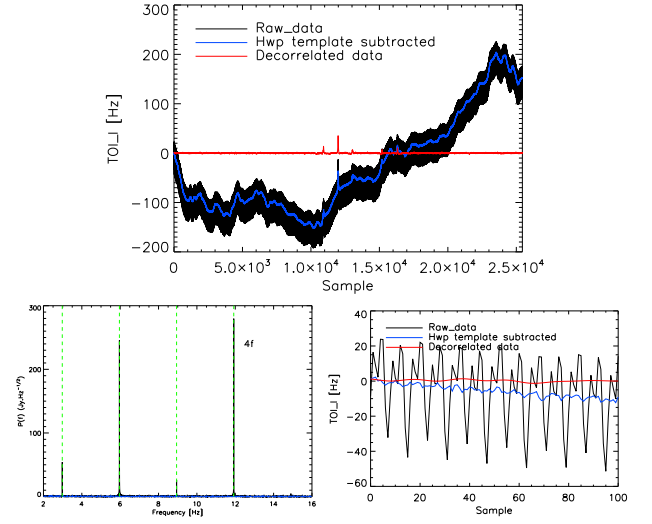


**Figure 5.** Time ordered information Stokes vector  $I$  for a KID and a scan of Orion OMC-1. Raw data in black, subtracted data for the HWP template in blue and decor related data in red. Timeline for a KID on top and a zoomed part on bottom right. Power spectrum of the timeline on bottom left.

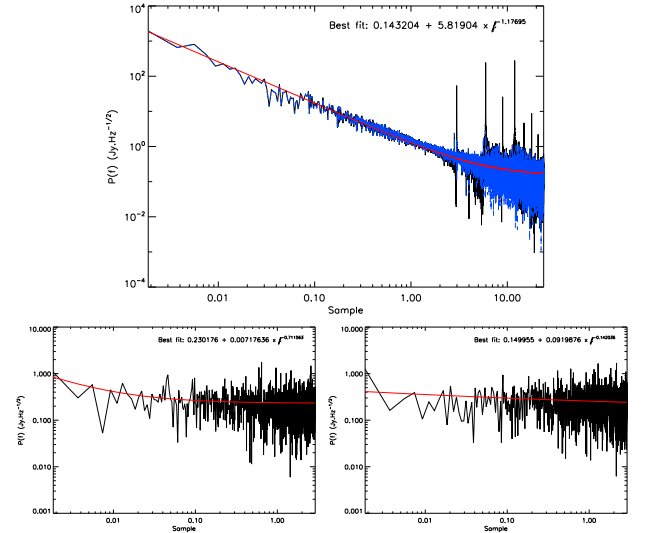


**Figure 6.** Intensity spectrum on top, the black line represents the raw data, blue line the data subtracted for the HWP template and the red line the fit. On the bottom we represent the data in polarization  $Q$  (left) and  $U$  (right) obtained after the lock-in procedure and cleaned by the HWP template.

## 6. Calibration at the telescope

### 6.1. Photometric calibration

During the polarization campaign on February the calibration procedure used was the same discussed in section 5, the *sky-dip* has been performed with the operating rotating HWP and the polarization pipeline has been used in order to have the TOI intensity Stokes vector  $I$ . The calibration factor includes the correction for the reduced flux received by the LEKIDs due to the wire-grid. In order to compare with other experiments we choose two of the quasars collection that we had, the quasars 3C273 and 3C286, indicated as primary flux calibrator. In fig. 7 we show the spectral density energy for the quasar 3C286, we plot the re-



sults obtained by PLANCK, ALMA, XPOL (Agudo et al. 2012) and NIKA (February 2015). The radio spectrum exhibits a synchrotron power law with a spectral index  $\beta \approx -1.007 \pm 0.033$ . The fig. 8 presents the PLANCK and NIKA results for the quasar 3C273, the spectrum shows two laws with spectral index  $\beta_1 \approx -0.3$  and  $\beta_2 \approx -0.7$ .

In order to cross check at the opacity correction and photometric calibration we compare the results of four (3C273, 1749+096, 0851+202, 0415+379) quasars observed by NIKA and XPOL experiment during parallel sessions of the observational campaign done in February 2015. In the tab. 1 we can see the consistency of NIKA results with XPOL observations.

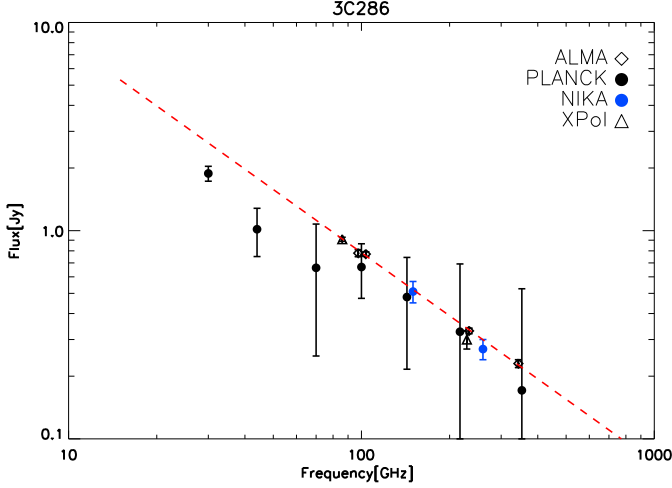


Figure 7. 3C286 SED of Planck, ALMA and NIKA .

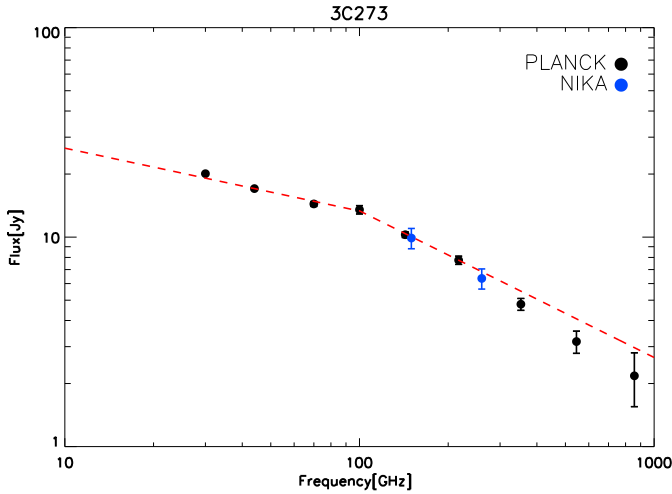


Figure 8. 3C273 SED of Planck, ALMA and NIKA .

## 6.2. Intensity to polarization leakage

Instrumental Polarization (IP) is the ability of the experimental setup to induce polarisation from an unpolarized incoming signal before the modulation by HWP. In order to estimate its level

at the telescope we have observed a planet, Uranus, which it is expected unpolarized. We identify a systematic effect fixed in NASMYTH coordinates. To first order we assume this effect as a leakage of total power into polarization. In terms of polarization degree the systematic effect corresponds to 2 % and 3 % of the intensity  $I$  at 2.05 mm and 1.15 mm, respectively. Let's call  $S_k$  the instantaneous measure of a kid and denote by a superscript  $N$  the Nasmyth coordinates, we have:

$$S_k = B_I * (I_0^N + Q_0^N \cos 2\alpha + U_0^N \sin 2\alpha) + L_{IQ} * I_0^N \cos 2\alpha + L_{IU} * I_0^N \sin 2\alpha + \text{noise} \quad (8)$$

where  $\alpha$  accounts for the HWP angle and sky coordinates rotation and  $B$  denotes the instrumental beam.  $L_{IX}$  the effective beam of the leakage. Uranus can be considered as a point source compared to NIKA's FWHM. The polarized observations of Uranus, once projected in Nasmyth coordinates are then exactly the point spread functions or beams  $L_{IQ}$  and  $L_{IU}$ . Our algorithm is thus:

1. Build a map of  $I$ ,  $Q$  and  $U$  of the observed source in R.A. and Dec. This map can be the combination of multiple scans to have the best signal to noise.
2. Rotate this map in Nasmyth coordinates to obtain  $I_N$ ,  $Q_N$  and  $U_N$ .
3. Deconvolve  $I_N$  from the instrumental beam to have an estimate of  $\hat{I}_0$  of the true intensity.
4. Use Uranus Nasmyth maps of  $Q$  and  $U$  as  $L_{IQ}$  and  $L_{IU}$  to convolve  $\hat{I}_0$  and produce maps of the expected leakage.
5. Scan these maps to produce timelines and subtract these timelines from the original data.
6. Projected these corrected data onto final maps.

The deconvolution/convolution steps 3 and 4 are performed at the same time in Fourier space:

$$(I_0^N * L_{IQ})(k) = I_0^N(k) \times L_{IQ}(k) \simeq I^N(k) / B_I(k) \times L_{IQ}(k) \quad (9)$$

The ratio  $L_{IQ}(k)/B_I(k)$  is tapered so that the division by decreasing terms of  $B_I(k)$  when  $k$  increases is counterbalanced by the deaming of  $L_{IQ}(k)$ . Once this correction is applied on Uranus polarisation maps the instrumental residual polarisation is  $< \sim 0.1$  %.

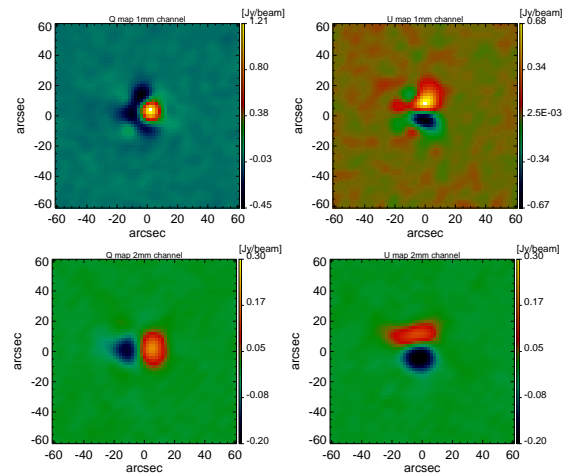


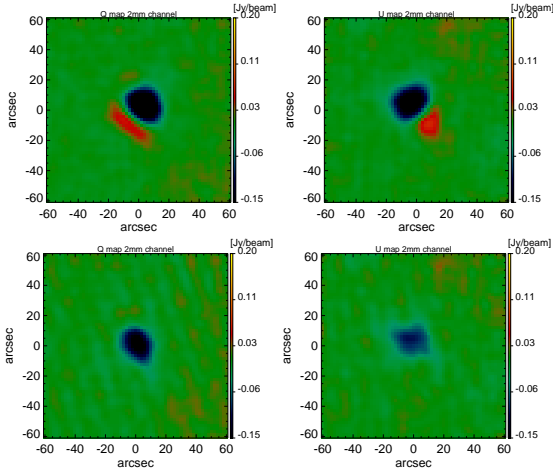
Figure 9. Q and U maps of Uranus (Nasmyth coordinates) showing the systematic effect at 1.25 mm (top) and 2.05 mm (bottom).

Let's take the quasar 3C273 as example. In the fig. 10 we show the Q and U maps without correction for the systematic

**Table 1.** Intensity flux by Xpol measurements on February 2015 vs *NIKA* observations

Source	I flux Xpol 1.25 mm [K]	I flux <i>NIKA</i> 1.25 mm [K]	I flux Xpol 3 mm [K]	I flux <i>NIKA</i> 2.05 mm [K]
3C273	$0.614 \pm 0.002$	$0.60 \pm 0.09$	$2.304 \pm 0.002$	$1.33 \pm 0.23$
1749+096	$0.201 \pm 0.001$	$0.15 \pm 0.03$	$0.558 \pm 0.001$	$0.26 \pm 0.06$
0851+202	$0.384 \pm 0.002$	$0.31 \pm 0.06$	$0.989 \pm 0.001$	$0.56 \pm 0.13$
0415+379	$0.117 \pm 0.002$	$0.122 \pm 0.025$	$0.343 \pm 0.000$	$0.235 \pm 0.054$

effect and after correction. The maps are projected in RA, Dec coordinates, we can see how the systematic effect produce a fake signal in the polarized maps and how our algorithm can correct for this.


**Figure 10.** Q and U maps of quasar 3C273 (RA, Dec coordinates) at 2.05 mm without leakage correction (top) and after correction on the bottom.

for the primary calibration source, the quasar 3C286 and  $\alpha_{sky} = (35.9 \pm 3.2)^\circ$  and  $\alpha_{sky} = (31.9 \pm 3.6)^\circ$  for the quasar 3C279.

In the table 3 we show the results obtained for the quasars (3C273, 1749+096, 0851+202, 0415+379) compared to the XPOL measurements. In the table 4 we report the results on polarization by other experiments in order to compare the performance of the *NIKA* polarimetry instrument.

### 6.3. Calibration on Quasars

During the observational campaign on February 2015 we have chosen a set of quasars with known polarization degree and angle in order to calibrate the *NIKA* polarimeter. The polarization degree  $p$  is defined by  $\sqrt{(Q^2 + U^2)}/I$  and the polarization angle  $\alpha_{sky}$  is equal to  $0.5 \arctan(U/Q)$  with the  $I$ ,  $Q$  and  $U$  maps. The quasar 3C286 is indicated as a primary calibrator and it has been observed by Xpol Agudo et al. (2012) and recently by CARMA Hull & Plambeck (2015) at 1.3 mm. XPol measures a flux density  $S_{3mm} = (0.91 \pm 0.02)$  Jy, a linear polarization degree  $p_{3mm} = [13.5 \pm 0.3] \%$  and a polarization angle  $\chi_{3mm} = [37.3 \pm 0.8]^\circ$ . Furthermore, it measures at 1mm a flux density  $S_{1mm} = [0.30 \pm 0.03]$  Jy, a polarization fraction  $p_{1mm} = [14.4 \pm 1.8] \%$  and a polarization angle  $\chi_{1mm} = [33.1 \pm 5.7]^\circ$ . The quasar 3C286 has been monitored by XPol from 2006 to 2012. It is presented as a calibration source at 3mm and at shorter wavelength. The recently observation at 1.3 mm by CARMA shows an angle  $\chi_{1.3mm} = [39.2 \pm 1]^\circ$ . The results at both frequencies in terms of flux, polarization degree and angle obtained on all quasars observed by *NIKA* are listed in the table 2. In particular we found a polarization angle at 260 GHz and 150 GHz, respectively, of  $\alpha_{sky} = (-89.3 \pm 3.2)^\circ$  and  $\alpha_{sky} = (-74.1 \pm 3.9)^\circ$  for the quasar 3C273,  $\alpha_{sky} = (29.0 \pm 3.9)^\circ$  and  $\alpha_{sky} = (27.7 \pm 3.9)^\circ$

Source	I flux [Jy]	Q flux [Jy]	U flux [Jy]	p [%]	$\alpha_{sky}$ [°]	I flux [Jy]	Q flux [Jy]	U flux [Jy]	p [%]	$\alpha_{sky}$ [°]
	260 GHz	260 GHz	260 GHz	260 GHz	260 GHz	150 GHz	150 GHz	150 GHz	150 GHz	150 GHz
3C279	8.51±0.97	0.260±0.005	0.79±0.09	9.8 ± 2.2	35.9±3.2	12.2±1.4	0.5±0.06	1.04±0.12	9.5±2.2	31.9±3.6
3C273	6.3 ±0.7	-0.22 ± 0.01	-0.009 ±0.001	3.8±0.4	-88.6±2.0	9.9 ±1.1	-0.17± 0.02	-0.10± 0.01	2.0 ± 0.5	-74.1 ± 3.9
3C286	0.27±0.03	0.020±0.002	0.033±0.004	14.1±3.2	29.0±3.9	0.5±0.1	0.037±0.004	0.05±0.01	12.9±2.9	27.7±3.9
3C345	1.08±0.12	0.035±0.002	0.003±0.004	3.2±0.7	2.7±2.2	1.8 ± 0.2	0.031±0.003	0.010±0.001	1.8±0.4	9.2±3.2
1749+096	1.64±0.19	0.005±0.004	0.063±0.007	3.9±0.9	43.0±2.1	1.9±0.2	-0.0016±0.0002	0.07±0.01	3.6±0.8	45.6± 1.9
0851+202	3.27±0.37	-0.105±0.002	0.02±0.002	3.3±0.7	84.0±2.7	4.3±0.5	-0.10±0.01	0.08±0.01	2.9 ± 0.7	70.3 ±4.1
0923+392	2.04±0.23	-0.002 ±0.005	-0.07 ± 0.01	3.3±0.7	-45.8±1.9	3.2±0.4	-0.016±0.002	-0.09 ± 0.01	2.7±0.6	-50.3±2.6
0415+379	1.29±0.15	0.017±0.006	-0.025±0.003	2.4±0.5	-28.4±3.9	1.8±0.2	0.010±0.001	-0.028±0.003	1.7±0.4	-34.2±3.4

**Table 2.** Intensity and polarization fluxes, polarisation degree and angle for the quasars observed at 260 GHz and at 150 GHz during the campaign on February 2015.

Source	P [%]	P [%]	P [%]	P [%]	$\alpha_{sky}$ [°]	P [%]	$\alpha_{sky}$ [°]	P [%]	$\alpha_{sky}$ [°]	P [%]	$\alpha_{sky}$ [°]
	NIKA 1.25 mm	XPOL 1.3 mm	NIKA 2.05 mm	XPOL 3 mm	NIKA 1.25 mm	XPOL 1.3 mm	NIKA 2.05 mm	XPOL 3 mm	NIKA 1.3 mm	NIKA 2.05 mm	XPOL 3 mm
3C273	3.3±0.4	3.6±0.2	1.9 ± 0.3	1.1± 0.0	-89.3±3.2	-76.8± 1.6	-73.7 ± 3.2	-37.8± 0.9			
1749+096	3.9±0.8	2.0±0.3	3.6±0.6	0.9±0.1	43.0±5.1	-83.0±3.7	45.6± 5.2	75.0±1.6			
0851+202	3.3±0.3	2.8±0.3	2.9 ± 0.4	1.1±0.0	83.98±3.84	-67.5±2.4	70.3 ±3.4	-38.5±1.7			
0415+379	2.4±1.0	2.2±1.5	1.7±0.5	0.4±0.1	-28.4±10.7	74.2 ±19.3	-34.2±6.3	-14.2 ±7.2			

**Table 3.** Polarization degree and angle for the quasars 3C273, 1749+096, 0851+202, 0415+379 by Xpol measurements on February 2015 vs NIKA observations.

Source	Experiment	Wavelength	P [%]	$\alpha_{sky}$ [°]	Observation date	Comments
3C279	SHARP Polarimeter	350 $\mu$ m, (3,5, 7, 13) mm	10 %-12 %	32-41	2014, March	Variable source
	NIKA	1.25 mm	9.4 ±0.7	35.8 ±2.4	2015, February	
3C286	NIKA	2.05 mm	9.2 ±1.16	32.4±2.9	2015, February	
	XPOL	1.3 mm	14.4 ± 1.8	33.1 ±5.7	2006-2012	Calibration source
	CARMA	1.3 mm		39.1± 1	2015, May	
	NIKA	1.25 mm	13.9 ± 2.4	29.0 ± 4.1	2015, February	
	NIKA	2.05 mm	12.4 ± 1.6	27.7 ±3.1	2015, February	
3C273	XPOL	3 mm	13.5 ±0.3	37.3 ±0.8	2006-2012	Observational parallel session
	XPOL	1.3 mm	3.6 ±0.2	-76.8±1.6	2015, February	
	NIKA	1.25 mm	3.3±0.4	-89.3±3.2	2015, February	
	NIKA	2.05 mm	1.9±0.2	-73.7±3.2	2015, February	
	XPOL	3 mm	1.1±0.0	-37.8±0.9	2015, February	

**Table 4.** Comparison of NIKA results with other experiments.

## 7. Extended sources observations

The systematic effect correction has been applied at the observations of several extended sources as Orion OMC-1, M87. The Orion Molecular Cloud (OMC) is the closest region of high-mass star-formation to the Sun, at  $\sim 450$  pc, and has consequently been much studied. The most prominent region in maps of the molecular gas is the OMC1 cloud, which contains several luminous star-forming cores Chini et al. (1997) and a large number of young stars. Comparing with SCUBA observation at  $850 \mu\text{m}$  shown in the fig. 11, where the contours represent the NIKA map at  $1.15 \text{ mm}$ , we find that the NIKA map is a bit shifted maybe because of some pointing error during the observation. We can compare this observation with NIKA observations at  $1.15$  and  $2.05 \text{ mm}$  shown in fig. 12 and compare the SCUBA intensity polarisation (fig. 11) with the NIKA intensity polarisation (fig. 14). The peak flux of the OMC1 emission in the Orion A molec-

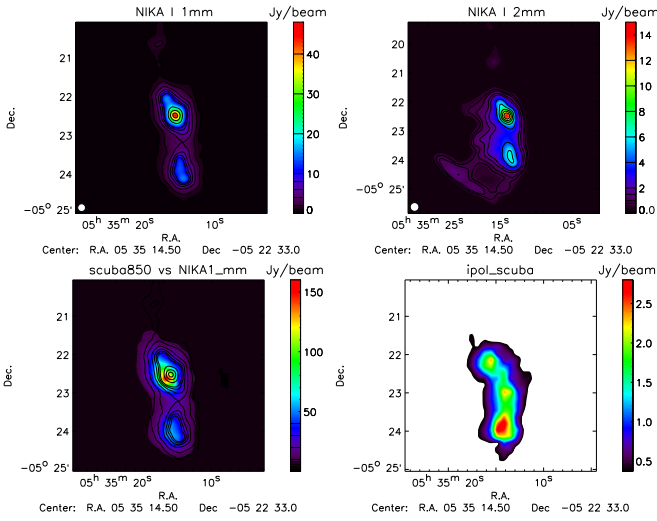


**Figure 11.** NIKA intensity maps of Orion OMC-1 at  $1.15 \text{ mm}$  (top left) and  $2.05 \text{ mm}$  (top right). SCUBA intensity map (bottom left) and polarisation intensity map (bottom right) at  $850 \mu\text{m}$  with NIKA  $1.15 \text{ mm}$  map contours. The contours represent the intensity  $I$  for each wavelength. In the  $1.15 \text{ mm}$  maps the contours range start from  $1 \text{ Jy/beam}^{-1}$  with steps of  $2 \text{ Jy/beam}^{-1}$  and then with  $10 \text{ Jy/beam}^{-1}$ . In the  $1.15 \text{ mm}$  maps the contours range start from  $0.8 \text{ Jy/beam}^{-1}$  with steps of  $0.2 \text{ Jy/beam}^{-1}$ , then of  $0.5 \text{ Jy/beam}^{-1}$  and then of  $2 \text{ Jy/beam}^{-1}$ .

ular cloud is about  $45.8 \text{ Jy/beam}$  and  $14 \text{ Jy/beam}$  at  $1.15 \text{ mm}$  and  $2.05 \text{ mm}$  respectively. The calibration error is reported as  $\sim 10 \%$ , see paper (Catalano et al. 2014). The polarisation angle and degree calculated with the average of the Stokes parameters are  $\alpha_{sky} = (21.3 \pm 3.6)^\circ$  and  $p = (4.0 \pm 0.8) \%$  and  $\alpha_{sky} = (22.1 \pm 2.6)^\circ$  and  $p = (6.0 \pm 0.9) \%$  at  $2.05 \text{ mm}$  and  $1.15 \text{ mm}$ , respectively. This is in agree with previous observations (Wiesemeyer et al. 2014). Intensity maps at  $1.15 \text{ mm}$  and  $2.05 \text{ mm}$  and polarisation intensity at  $2.05 \text{ mm}$  are presented in fig. 15. We don't detect polarisation at  $1.15 \text{ mm}$ . In the fig. 16 the intensity map with polarisation vectors at  $2.05 \text{ mm}$  is shown.

## 8. Conclusions

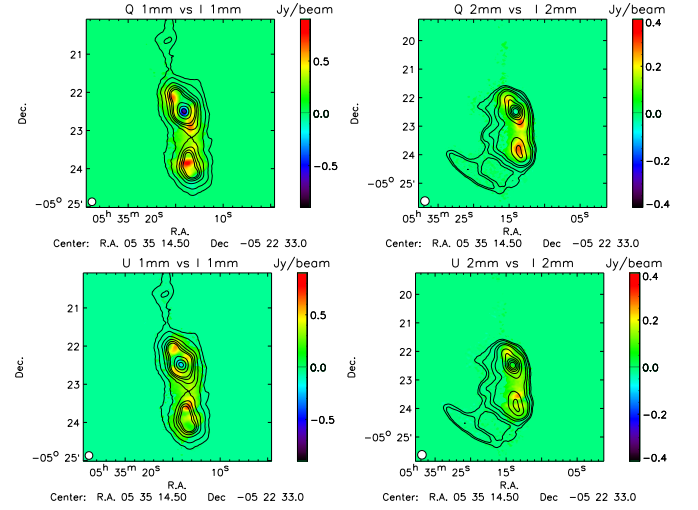


**Figure 12.** From the top to bottom vectors Stokes Q, U maps at  $1.15 \text{ mm}$  and  $2.05 \text{ mm}$  respectively of Orion OMC-1.

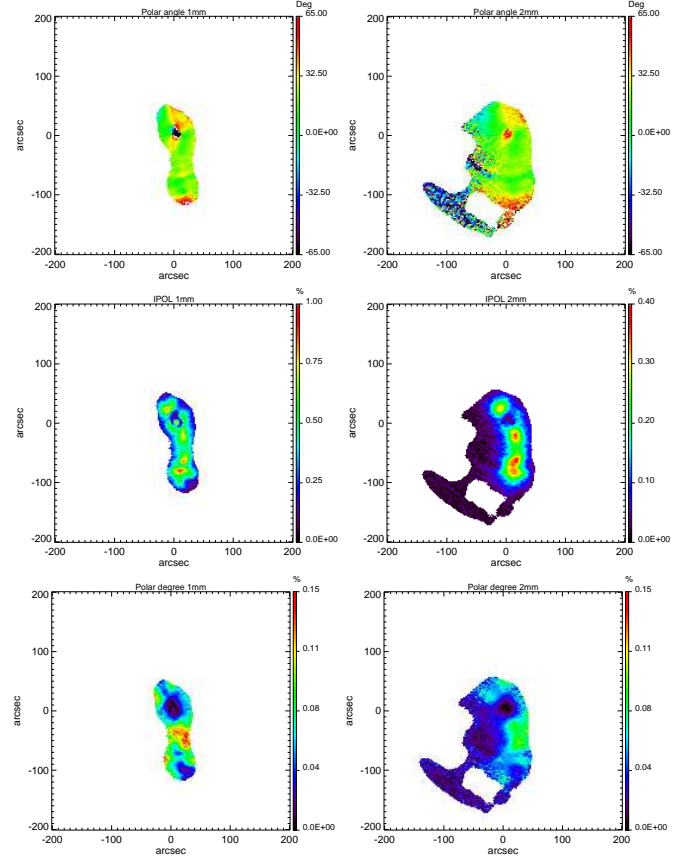


**Figure 13.** From the top to bottom angle, polarisation intensity and polarisation degree maps at  $1.15 \text{ mm}$  and  $2.05 \text{ mm}$  respectively of Orion OMC-1.

## References

- Adam, R. et al. 2014, A&A, 569, A66, 1310.6237
- Agudo, I., Thum, C., Wiesemeyer, H., Molina, S. N., Casadio, C., Gómez, J. L., & Emmanoulopoulos, D. 2012, A&A, 541, A111, 1201.2150
- Benoît, A. et al. 2004, A&A, 424, 571, astro-ph/0306222
- Catalano, A. et al. 2014, A&A, 569, A9, 1402.0260
- Chini, R., Reipurth, B., Ward-Thompson, D., Bally, J., Nyman, L.-Å., Sievers,



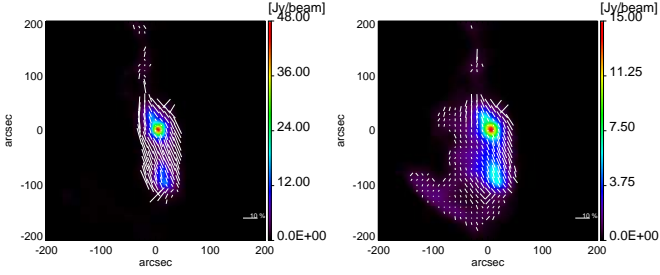


**Figure 14.** Intensity map at 1.15 mm (left) and 2.05 mm (right) respectively with polarisation vectors.

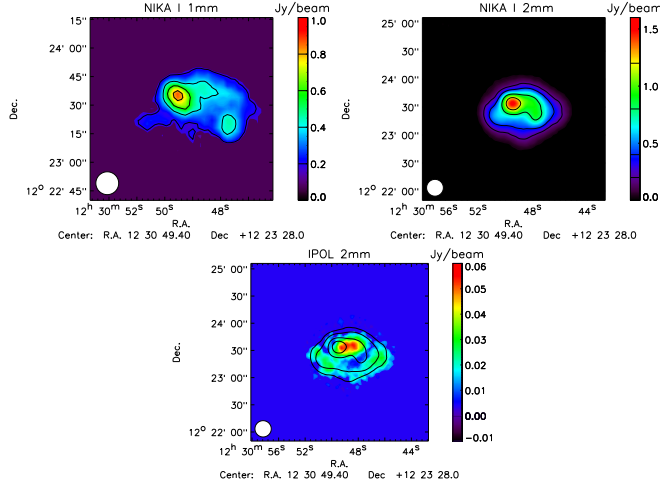


**Figure 15.** M87 maps. On the top intensity maps at 1.15 mm and 2.05 mm respectively. On bottom polarisation intensity at 2.05 mm, we don't detect polarisation at 1.15 mm.

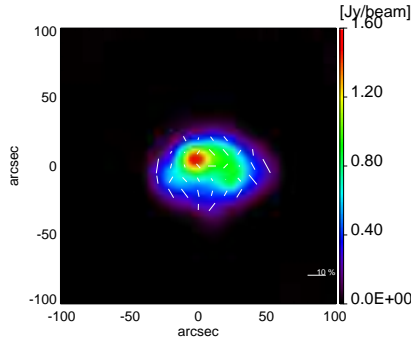


**Figure 16.** M87 intensity Stokes vector I with polarisation vectors at 2.05 mm.

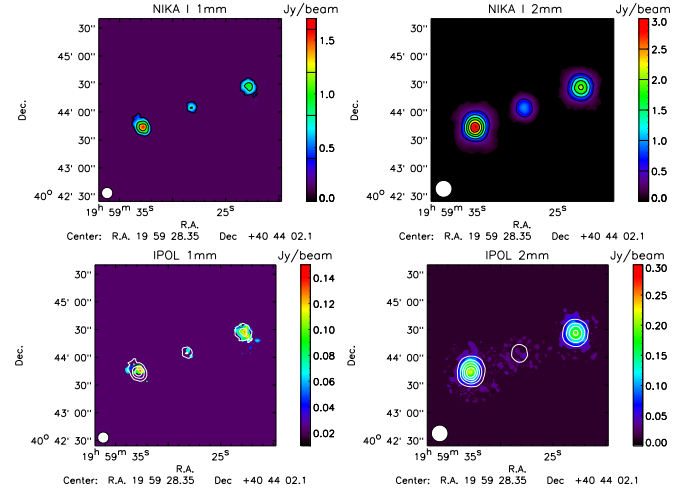


**Figure 17.** Cygnus A maps. Intensity maps (top) and polarisation intensity (bottom) at 1.15 mm and 2.05 mm respectively.

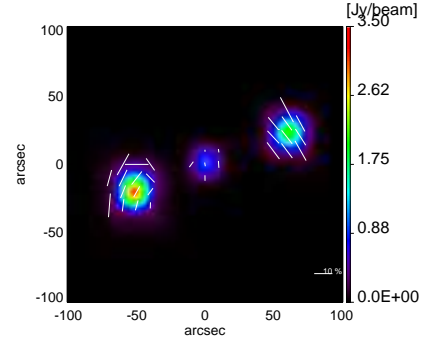


**Figure 18.** Cygnus A intensity Stokes vector I with polarisation vectors at 2.05 mm.

Siringo, G., Kreysa, E., Reichertz, L. A., & Menten, K. M. 2004, A&A, 422, 751  
Wiesemeyer, H. et al. 2014, PASP, 126, 1027, 1408.5100

A., & Billawala, Y. 1997, ApJ, 474, L135  
Dicke, R. H., Beringer, R., Kuhl, R. L., & Vane, A. B. 1946, Phys. Rev., 70, 340  
Doyle, S. et al. 2008, in Society of Photo-Optical Instrumentation Engineers (SPIE) Conference Series, Vol. 7020, Society of Photo-Optical Instrumentation Engineers (SPIE) Conference Series, 0  
Fiege, J. D., & Pudritz, R. E. 2000, ApJ, 544, 830, astro-ph/0005363  
Hull, C. L. H., & Plambeck, R. L. 2015, Journal of Astronomical Instrumentation, 4, 50005, 1506.04771  
Johnson, B. R. et al. 2007, ApJ, 665, 42, astro-ph/0611394  
Matthews, B. C., Fiege, J. D., & Moriarty-Schieven, G. 2002, ApJ, 569, 304, astro-ph/0201347  
Monfardini, A. et al. 2010, A&A, 521, A29, 1004.2209  
Roesch, M. et al. 2012, ArXiv e-prints, 1212.4585  
Savini, G., Pisano, G., & Ade, P. A. R. 2006, Appl. Opt., 45, 8907